Supporting Information for:

Developing efficient catalysts for OER and ORR using a combination of Co, Ni, and Pt oxides along with graphene nanoribbon and $NiCo_2O_4$

*Leticia S. Bezerra and Gilberto Maia**

Institute of Chemistry, Federal University of Mato Grosso do Sul; Av. Senador Filinto Muller, 1555; Campo Grande, MS 79074-460, Brazil

*Corresponding Author. E-mail: gilberto.maia@ufms.br

Tel.: +55 67 3345 3551. Fax: +55 67 3345 3552.

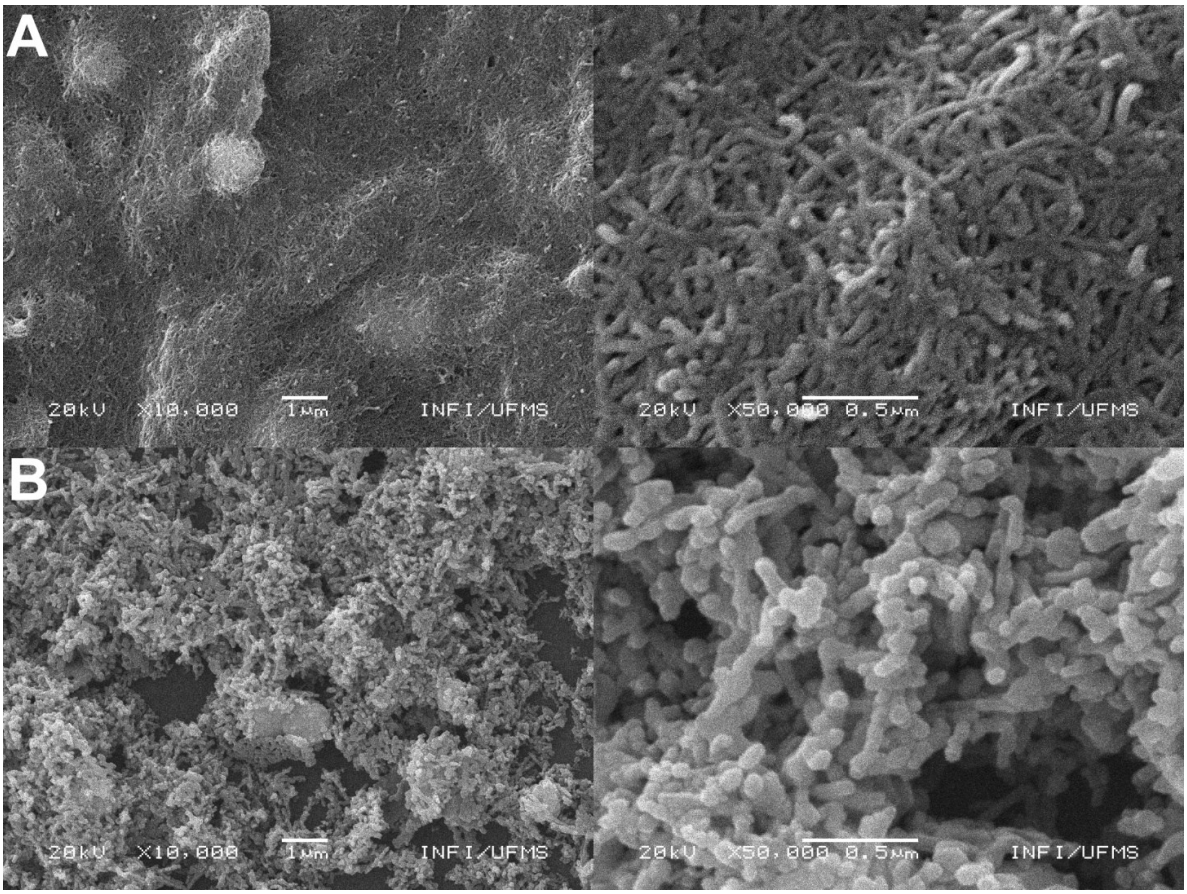

Figure S1. SEM images for non-electrochemically stabilized PtCoNi/GNR (A) and $NiCo_2O_4$ (B) nanocomposites and nanoparticles ($NiCo_2O_4$) dripped as a film at FTO support.

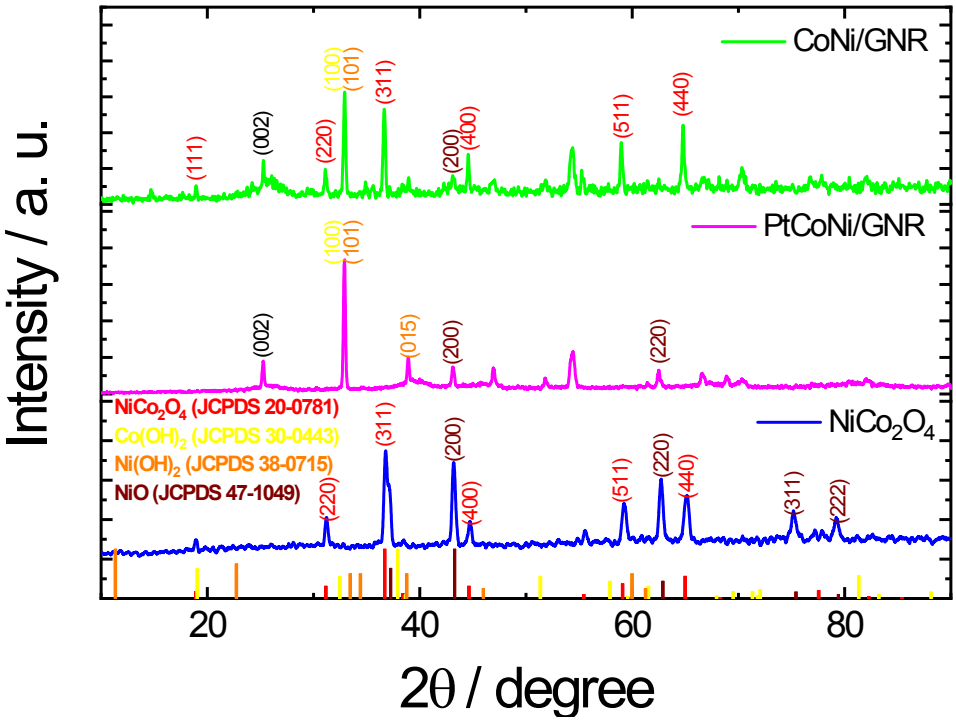

Figure S2. XRD patterns for non-electrochemically stabilized CoNi/GNR, PtCoNi/GNR, and $NiCo_2O_4$ nanocomposites and nanoparticles ($NiCo_2O_4$).

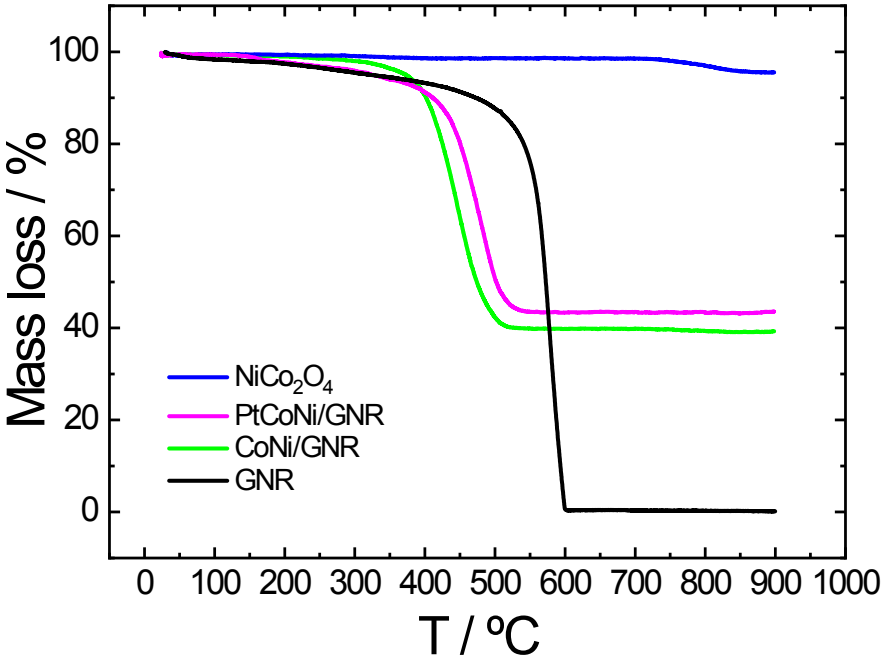

Figure S3. TG curves for non-electrochemically stabilized CoNi/GNR, PtCoNi/GNR, and $NiCo_2O_4$ nanocomposites and nanoparticles ($NiCo_2O_4$).

Table S1. CHN analyses, wt.%.

Catalysts	Elements		
	N	C	H
$NiCo_2O_4$	<0.05	<0.05	<0.05

Table S2. Results from atomic emission spectroscopy analysis, wt.%.

Catalyst	Elements		
	Co	Ni	Pt
$NiCo_2O_4$	40	36	-

Table S3. EDX and TG metal masses (unburned) and TG and EDX mass percentages for non-electrochemically stabilized CoNi/GNR, PtCoNi/GNR, and $NiCo_2O_4$ nanocomposites and nanoparticles ($NiCo_2O_4$).

Catalyst	EDX metal mass (%)	TG metal mass (mass unburned) (%)	TG and EDX mass (%)
$NiCo_2O_4$	40.9 Co 37.0 Ni	0	-
CoNi/GNR	38.3 Co 33.7 Ni	40.0	60 C 11.2 O 15.3 Co 13.5 Ni
PtCoNi/GNR	28.5 Co 29.7 Ni 20.6 Pt	43.5	56.5 C 9.2 O 12.4 Co 12.9 Ni 9.0 Pt

O mass % completes the total EDX mass %.

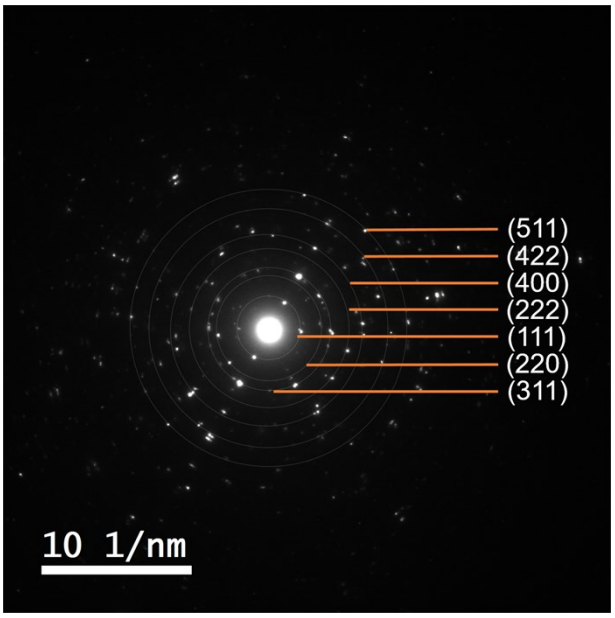

Figure S4. Electron diffraction patterns for electrochemically stabilized (after OER) $NiCo_2O_4$ nanoparticles.

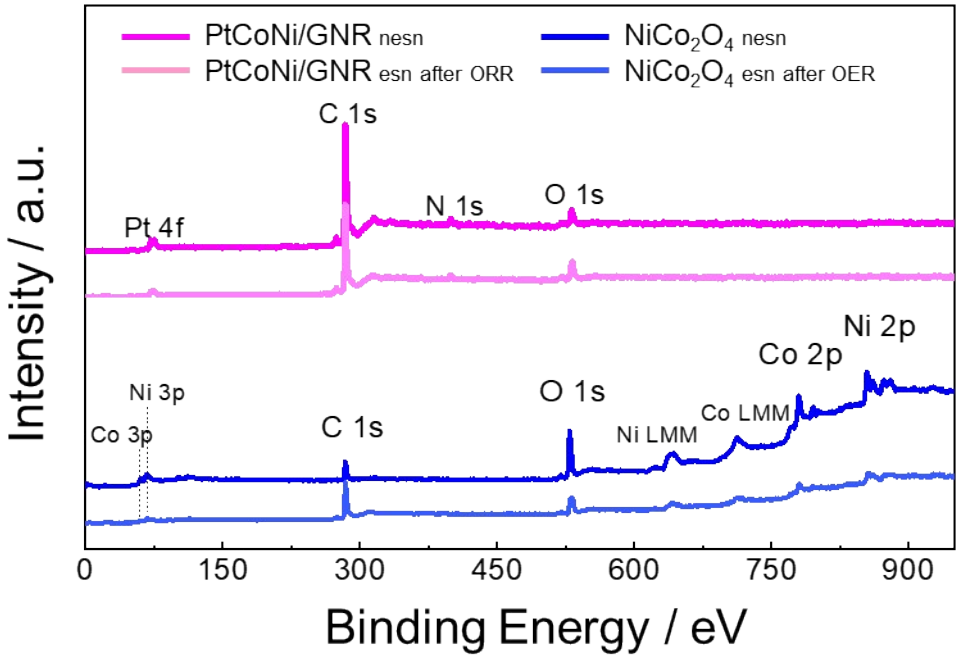

Figure S5. XPS survey spectrum for non-electrochemically and electrochemically stabilized PtCoNi/GNR and $NiCo_2O_4$ nanocomposites and nanoparticles ($NiCo_2O_4$). nesn = non-electrochemically stabilized nanocomposites or nanoparticles and esn = electrochemically stabilized nanocomposites or nanoparticles.

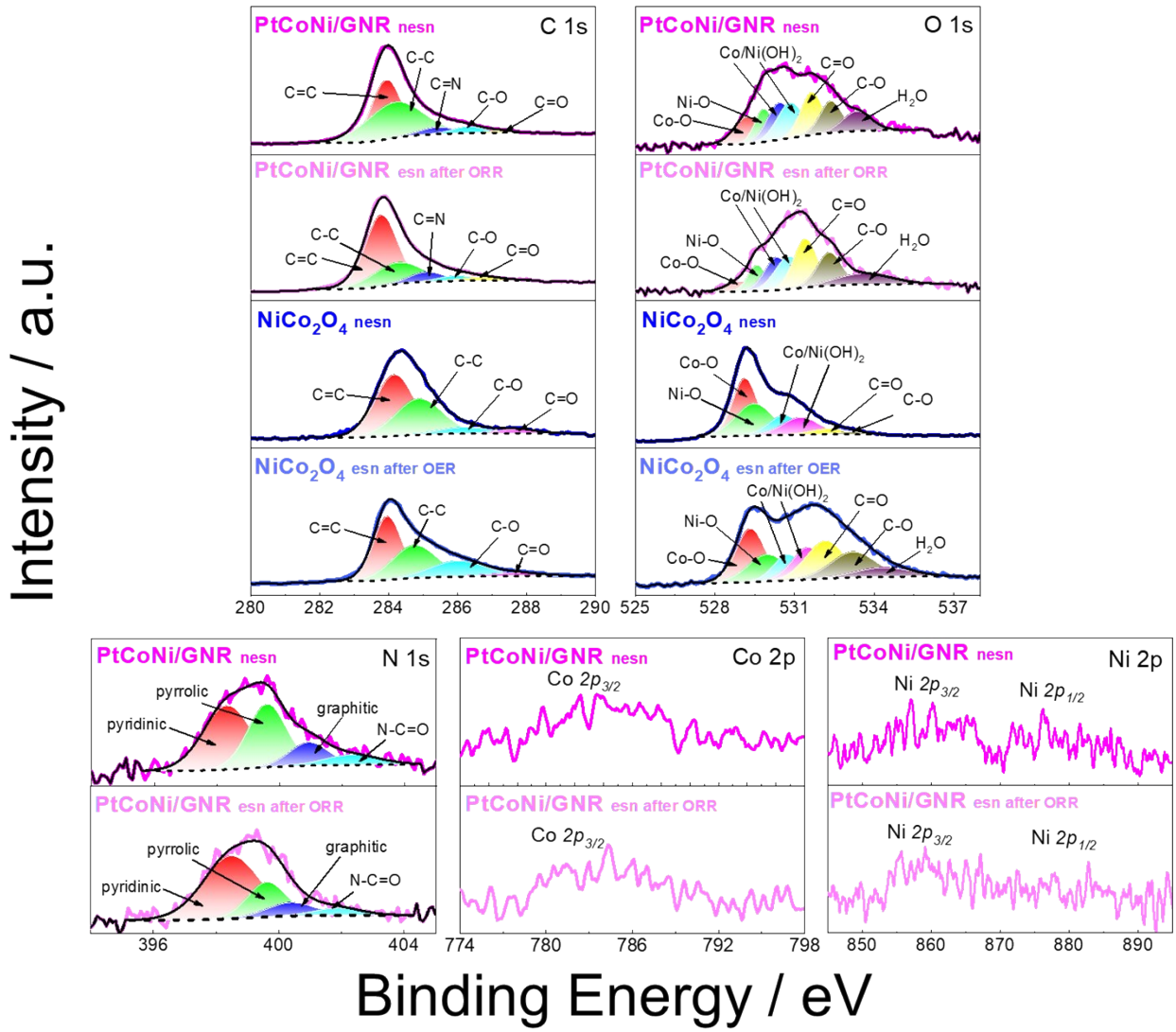

Figure S6. High resolution XPS of C 1s, O 1s, N 1s, Co 2p, and Ni 2p for the synthesized catalyst regions. nesn = non-electrochemically stabilized nanocomposites or nanoparticles and esn = electrochemically stabilized nanocomposites or nanoparticles.

Table S4 – Positions, relative sensitive factors (R.S.F.), atomic and mass percentages obtained from the XPS spectra shown in Figure S5 for non-electrochemically and electrochemically stabilized PtCoNi/GNR and $NiCo_2O_4$ nanocomposites and nanoparticles ($NiCo_2O_4$). nesn = non-electrochemically stabilized nanocomposites or nanoparticles and esn = electrochemically stabilized nanocomposites or nanoparticles.

Catalyst	Name	Position (eV)	R.S.F.	Atomic %	Mass %
PtCoNi/GNR nesn	O 1s	531.00	2.93	5.85	6.60
	C 1s	284.00	1	89.62	75.81
	N 1s	399.00	1.8	3.50	3.45
	Pt 4f	72.00	15.5	1.03	14.13
PtCoNi/GNR esn after ORR	O 1s	532.00	2.93	9.75	11.45
	C 1s	284.00	1	86.57	76.32
	N 1s	398.00	1.8	3.05	3.13
	Pt 4f	74.00	15.5	0.64	9.11
$NiCo_2O_4$ nesn	O 1s	529.00	2.93	45.17	35.43
	C 1s	284.00	1	40.76	24.00
	Co 2p	780.00	19.2	7.69	22.22
	Ni 2p	854.00	22.2	6.37	18.34
$NiCo_2O_4$ esn after OER	O 1s	532.00	2.93	18.34	18.31
	C 1s	284.00	1	74.65	55.96
	Co 2p	780.00	19.2	3.18	11.70
	Ni 2p	855.00	22.2	3.83	14.03

Tabela S5 – Positions and percentages of the content of functional groups present in non-electrochemically and electrochemically stabilized PtCoNi/GNR and $NiCo_2O_4$ nanocomposites and nanoparticles ($NiCo_2O_4$) obtained from high-resolution XPS spectra shown in Figures 2 and S6.

Catalyst	Name	Group	Position (eV)	% content
PtCoNi/GNR non-electrochemically stabilized nanocomposites	O 1s	Co−O	529.56	13.62
		Ni−O	530.21	11.09
		$Co(OH)_2$	530.86	16.89
		$Ni(OH)_2$	531.29	17.35
		C=O	532.16	17.78
		C−O	532.94	12.92
		H_2O	534.00	10.34
	C 1s	C=C	283.94	41.16
		C−C	284.19	47.36
		C=N	285.43	5.42
		C−O	286.31	4.78
		C=O	287.23	1.28
	N 1s	pyridinic	398.32	44.26
		pyrrolic	399.6	35.02
		graphitic	400.94	12.79
		N−C=O	402.32	7.93

	Pt 4f	Pt 0	70.74	23.04
		Pt 2+	71.94	25.39
		Pt 4+	73.59	8.71
		Pt 0	74.19	17.28
		Pt 2+	75.34	19.04
		Pt 4+	77.13	6.53
PtCoNi/GNR electrochemically stabilized nanocomposites after ORR	O 1s	Co−O	529.21	5.62
		Ni−O	529.94	9.37
		$Co(OH)_2$	530.74	15.97
		$Ni(OH)_2$	531.24	17.85
		C=O	531.9	22.94
		C−O	532.88	16.13
		H_2O	534.28	12.11
	C 1s	C=C	283.79	57.06
		C−C	284.27	26.46
		C=N	285.11	8.38
		C−O	285.97	4.54
		C=O	286.73	3.56
	N 1s	pyridinic	398.48	60.82
		pyrrolic	399.62	22.62
		graphitic	400.4	10.81
		N−C=O	401.88	5.76
	Pt 4f	Pt 0	70.58	16.69
		Pt 2+	71.85	29.12
		Pt 4+	73.67	11.88
		Pt 0	74.36	12.52
		Pt 2+	75.48	21.84
		Pt 4+	78.06	7.94
$NiCo_2O_4$ non-electrochemically stabilized nanoparticles	O 1s	Co−O	529.13	34.44
		Ni−O	529.47	29.01
		$Co(OH)_2$	530.61	14.65
		$Ni(OH)_2$	531.24	15.28
		C=O	532.28	4.91
		C−O	533.12	1.71
	C 1s	C=C	284.17	52.1
		C−C	284.89	37.25
		C−O	286.22	6.97
		C=O	287.73	3.67
	Co 2p	Co 3+	779.24	38.66
		Co 2+	780.97	28.27
		satellite	784.32	7.59
		Co 3+	794.26	12.16
		Co 2+	795.73	8.85
		Satellite	797.24	4.47
	Ni 2p	Ni 2+	853.83	14.43
		Ni 3+	855.77	21.96
		Satellite	860.21	14.83
		Satellite	862.78	11.33
		Ni 2+	871.81	11.21
		Ni 3+	874.29	9.03

		Satellite	878.59	11.22
		Satellite	881.66	5.98
$NiCo_2O_4$ electrochemically stabilized nanoparticles after OER	O 1s	Co−O	529.34	20.97
		Ni−O	529.96	13.94
		$Co(OH)_2$	530.75	9.99
		$Ni(OH)_2$	531.51	13.85
		C=O	532.16	19.33
		C−O	533.22	15.19
		H_2O	534.36	6.75
	C 1s	C=C	283.97	42.24
		C−C	284.76	34.08
		C−O	286.01	20.2
		C=O	287.75	3.48
	Co 2p	Co 3+	779.42	35.96
		Co 2+	781.19	27.08
		Satellite	783.02	14.65
		Co 3+	795.15	13.52
		Co 2+	797.15	6.61
		Satellite	799.54	2.18
	Ni 2p	Ni 2+	854.86	16.60
		Ni 3+	856.78	23.43
		Satellite	861.42	15.38
		Satellite	864.48	7.05
		Ni 2+	872.95	13.38
		Ni 3+	876.07	6.84
		Satellite	879.06	8.66
		Satellite	882.12	8.66

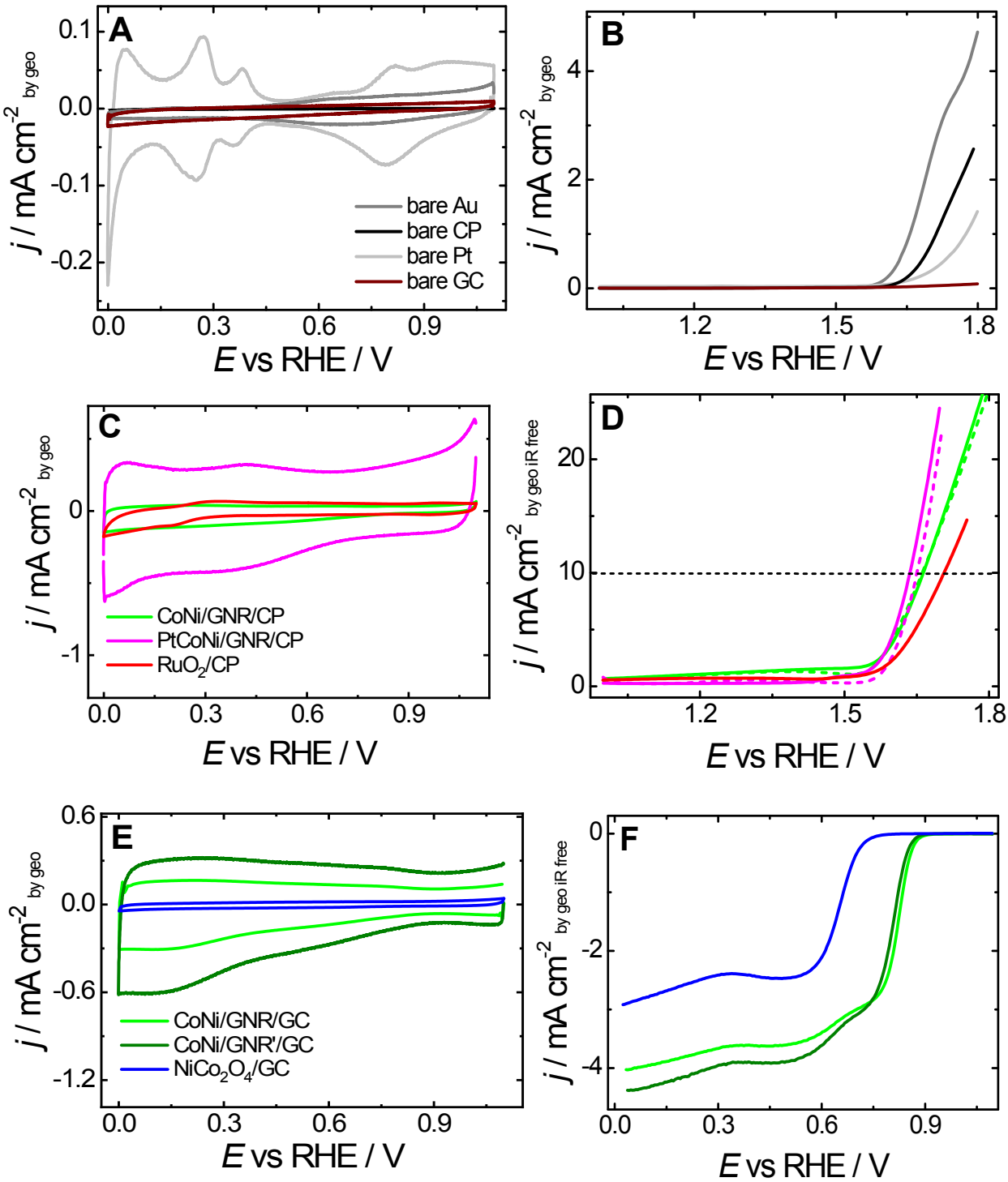

Figure S7. (A, C, and E) Cyclic voltammograms for different bare and modified electrodes. Potential scan rate: 50 mV s^{-1}, N_2-saturated 1 M KOH (A and C) and 0.1 M KOH (E). (B and D) Hydrodynamic linear voltammograms recorded for bare and different modified electrodes (stationary linear voltammetry is employed only when CP is used as substrate) in O_2-saturated 1 M KOH. ν: 5 mV s^{-1}, ω = 1600 rpm. Scans started at 1.1 V. (F) ORR curves for different

modified electrodes obtained in an O_2-satured 0.1 M KOH. Scan rate: 10 mV s^{-1} and ω=1600 rpm. Scans started at 0.00 V.

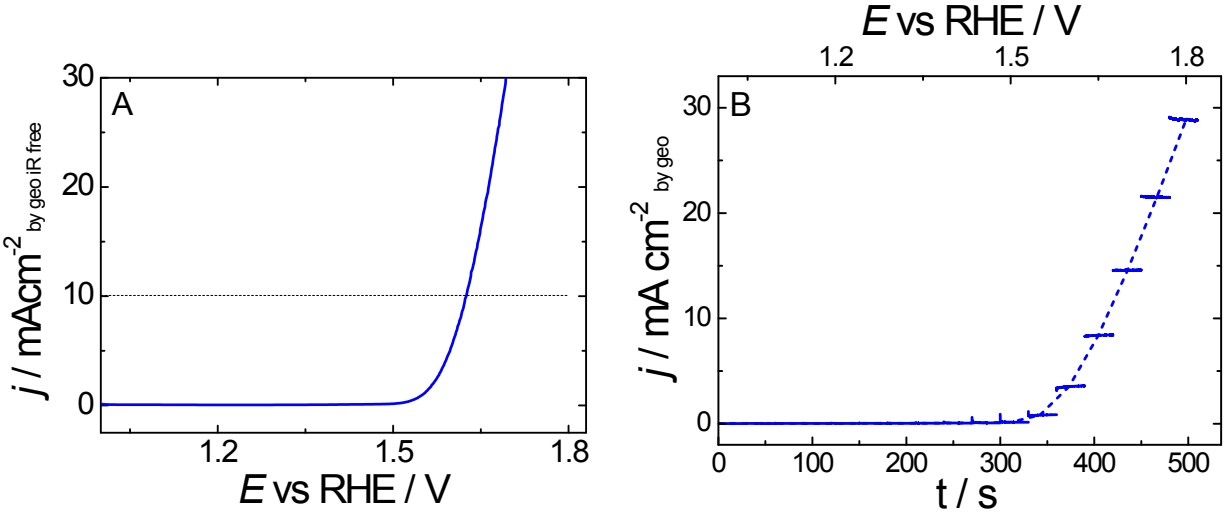

Figure S8. (A) Stationary linear voltammogram for $NiCo_2O_4$/CP electrode using O_2-saturated 1 M KOH. ν: 1 mV s^{-1}. Potential scan started at 1.0 V. (B) Chronoamperometric responses for $NiCo_2O_4$/CP electrode in O_2-saturated 1 M KOH. The potential was kept for 30 seconds in different potentials starting from 1.0 to 1.8 V with 0.05 V for each step. The dashed line was obtained from the chronoamperometric results at different steps by a chord-area plot and plotted as a function of time and potential.

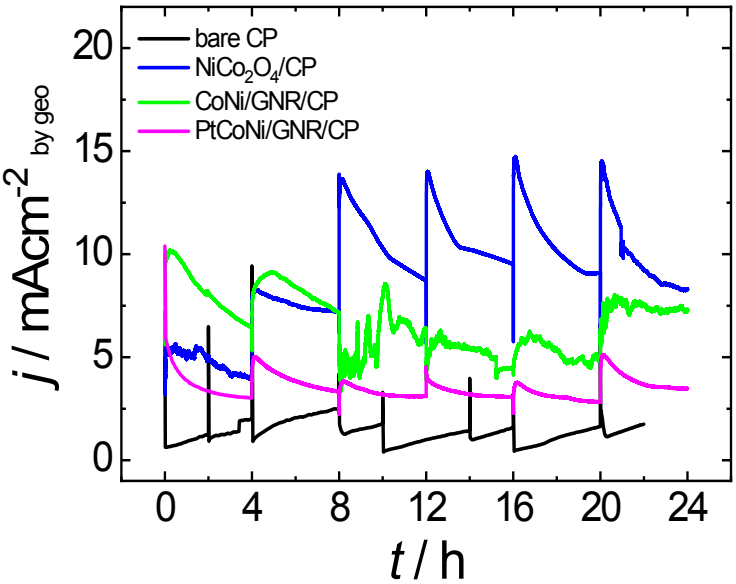

Figure S9. Chronoamperometries for bare and different modified CP electrodes at 1.67 V (potential: 10 mA $cm^{-2}_{by\ geo}$) obtained in O_2-saturated 1.0 M KOH solution.

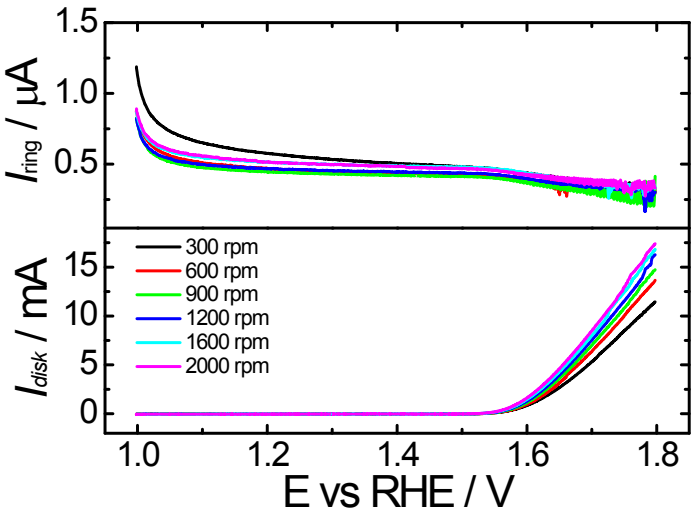

Figure S10. (A) Hydrodynamic linear potential scan (HLS) curves for $NiCo_2O_4$/Au disk electrode obtained in N_2-satured 1.0 M KOH. Scan rate: 5 mV s^{-1}. Scans started at 1.0 V. The ring current responses for the bare Pt ring were obtained by maintaining this electrode at 1.2 V in N_2 saturated 1.0 M KOH, while the potentials on the modified Au disk electrode were scanned in the same solution at various ω values and 5 mV s^{-1}.

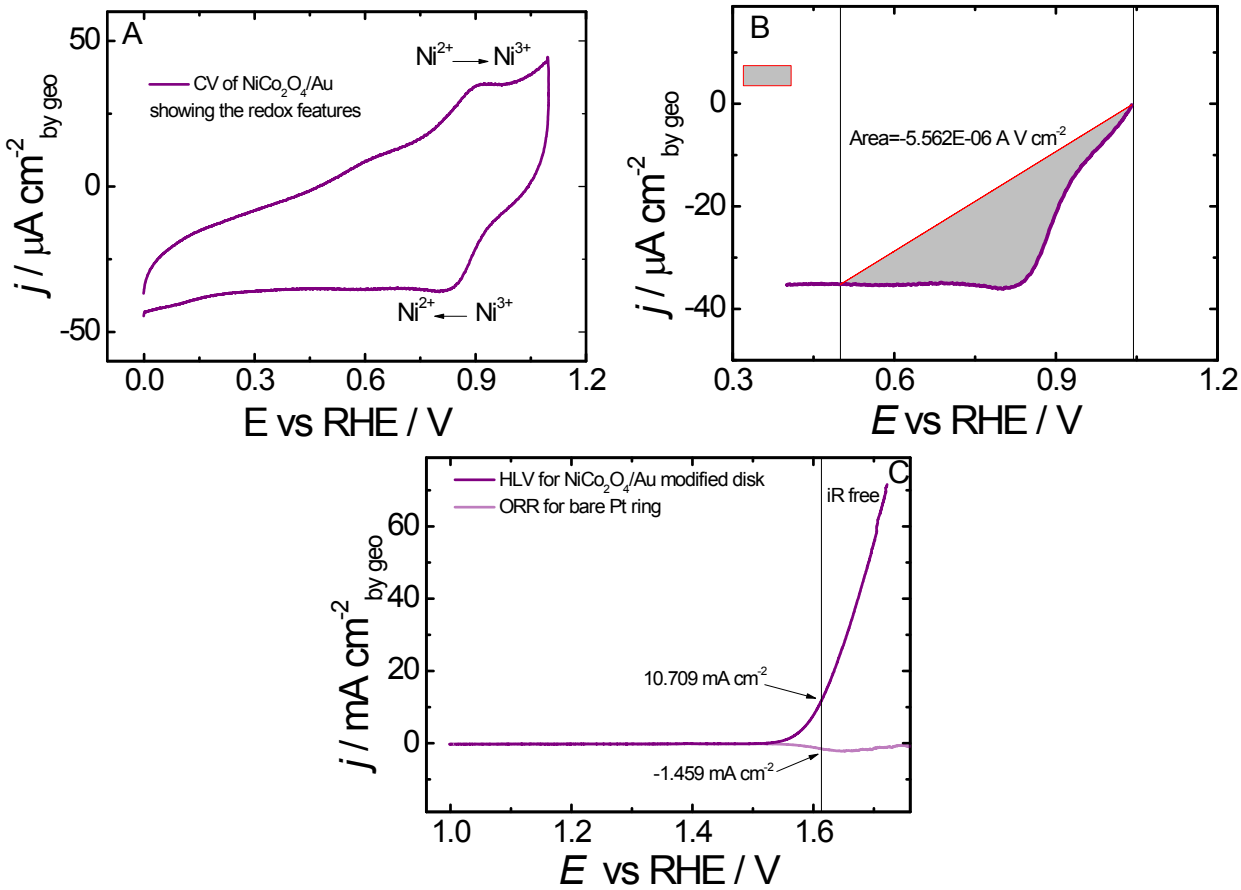

Figure S11. (A) Cyclic voltammogram for $NiCo_2O_4$/Au modified disk electrode in N_2-saturated 1 M KOH. Potential scan rate: 50 mV s^{-1}. Potential started at 1.1 V. (B) Amplified part of (A) showing the integrated area from reduction peaks used to determine Ni^{2+} surface active species. (C) Hydrodynamic linear potential scan for $NiCo_2O_4$/Au modified disk electrode obtained in N_2-satured 1.0 M KOH. Potential scan rate: 5 mV s^{-1} and ω=1600 rpm. Potential scan started at 1.0 V. The ring current response for the bare Pt ring was obtained by maintaining this electrode at 0.4 V in N_2-saturated 1.0 M KOH, while the potential on the modified Au disk electrode was scanned in the same solution at ω=1600 rpm and 5 mV s^{-1}.

Table S6 – Values related to content, double layer capacitance (C_{dl})—obtained from CV responses (Figure S12), electrochemically active surface area (ECSA)—obtained from (Figure S13), overpotential at 10 mA cm^{-2} of current density (η_j at 10 mA cm^{-2} from Figures 3B, S7B, and S7D), and Tafel slope for bare and modified electrodes (Figure S14).

Electrode	Loading (μg cm^{-2})	C_{dl} (μF)			ECSA (cm^2)			η_j at 10 mA cm^{-2} (V)	Tafel slope (mV dec^{-1})
		Initial	After OER	After OER stability	Initial	After OER	After OER stability		
Bare CP	-	0.7	7.2	-	0.02	0.2	-	-	-
$NiCo_2O_4$/CP	150	49.8	1,214	3,668	1.2	30.4	91.7	0.36	56
$NiCo_2O_4$/Au	150	10.62	9.52	43.06	0.26	0.24	1.07	0.35	56
$NiCo_2O_4$/Pt	150	9.93	42.71	820.83	0.24	1.06	20.52	0.36	56
$NiCo_2O_4$/GC	150	8.05	10.41	-	0.20	0.26	-	0.40	121
PtCoNi/GNR/CP	150	1,300	832.2	1,202	32.4	20.8	30.1	0.40	90
CoNi/GNR/CP	150	420.0	372.3	15,724	10.5	9.3	293.8	0.43	131
RuO_2/CP	150	695.8	175.4	-	17.4	4.4	-	0.47	133

Table S7. Summary for $NiCo_2O_4$ OER activity reported in the present study and earlier literature.

Catalyst	Loading (μg cm^{-2})	η_j at 10 mA cm^{-2} (V)	Tafel slope (mV dec^{-1})	Solution	Ref.
$NiCo_2O_4$	150	0.35	56	1 M KOH	**Present study**
$NiCo_2O_4$-R	714.3	0.36	106	1 M KOH	[1]
$NiCo_2O_4$ nanoplatelets	Not reported	0.32 (η_j at 100 mA cm^{-2})	54	1 M KOH	[2]
Three-dimensional $NiCo_2O_4$ core-shell nanowires	Not reported	0.32	47.4-63.1	1 M NaOH	[3]
HU-$NiCo_2O_4$	69	0.42	51.3	1 M NaOH	[4]
NWAs	200	Not reported	62	1 M KOH	[5]
Mixed NiO/$NiCo_2O_4$ nanocrystals	500	0.27	79.3	1 M KOH	[6]
3D porous $NiCo_2O_4$ nanosheets	200	0.38	63.4	0.1 M KOH	[7]
Spinel $NiCo_2O_4$ 3-D nanoflowers	25,500	0.38	137	1 M KOH	[8]
2D α-$Ni(OH)_2$	200	0.26	77.4	1 M KOH	[9]
Hierarchical $NiCo_2O_4$@$CoMoO_4$ nanowires/nanosheets	Not reported	0.27 (η_j at 20 mA cm^{-2})	102	1 M KOH	[10]
Co_3O_4 nanocages and $NiCo_2O_4$ nanosheets	1,000	0.32	84	0.1 M KOH	[11]
MOF-derived $NiCo_2O_4$/NiO and $NiCo_2O_4$/NiO-rGO	Not reported	0.39 and 0.34	49 and 66	1 M KOH	[12]
Porous $NiCo_2O_4$	194	0.30	70.3	6 M KOH	[13]
$NiCo_2O_{4-\delta}$	Not reported	Not reported	180	1 M NaOH	[24]
Porous nanoscale NiO/$NiCo_2O_4$ heterostructure	354	0.26	44.2	1 M KOH	[15]
Hierarchical $NiCo_2O_4$ hollow nanospheres	400	0.42 (η_j at 5 mA cm^{-2})	Not reported	0.1 M KOH	[16]
Spinel based $NiCo_2O_4$	394	0.35	43	1 M KOH	[17]
$NiCo_2O_4$ nanoframe	285	0.27	82	1 M KOH	[18]

$NiCo_2O_4$-R = $NiCo_2O_4$ obtained from the residual solution; HU-$NiCo_2O_4$ = hierarchical hollow urchins of $NiCo_2O_4$; NWAs = 1D $NiCo_2O_4$ nanowire arrays.

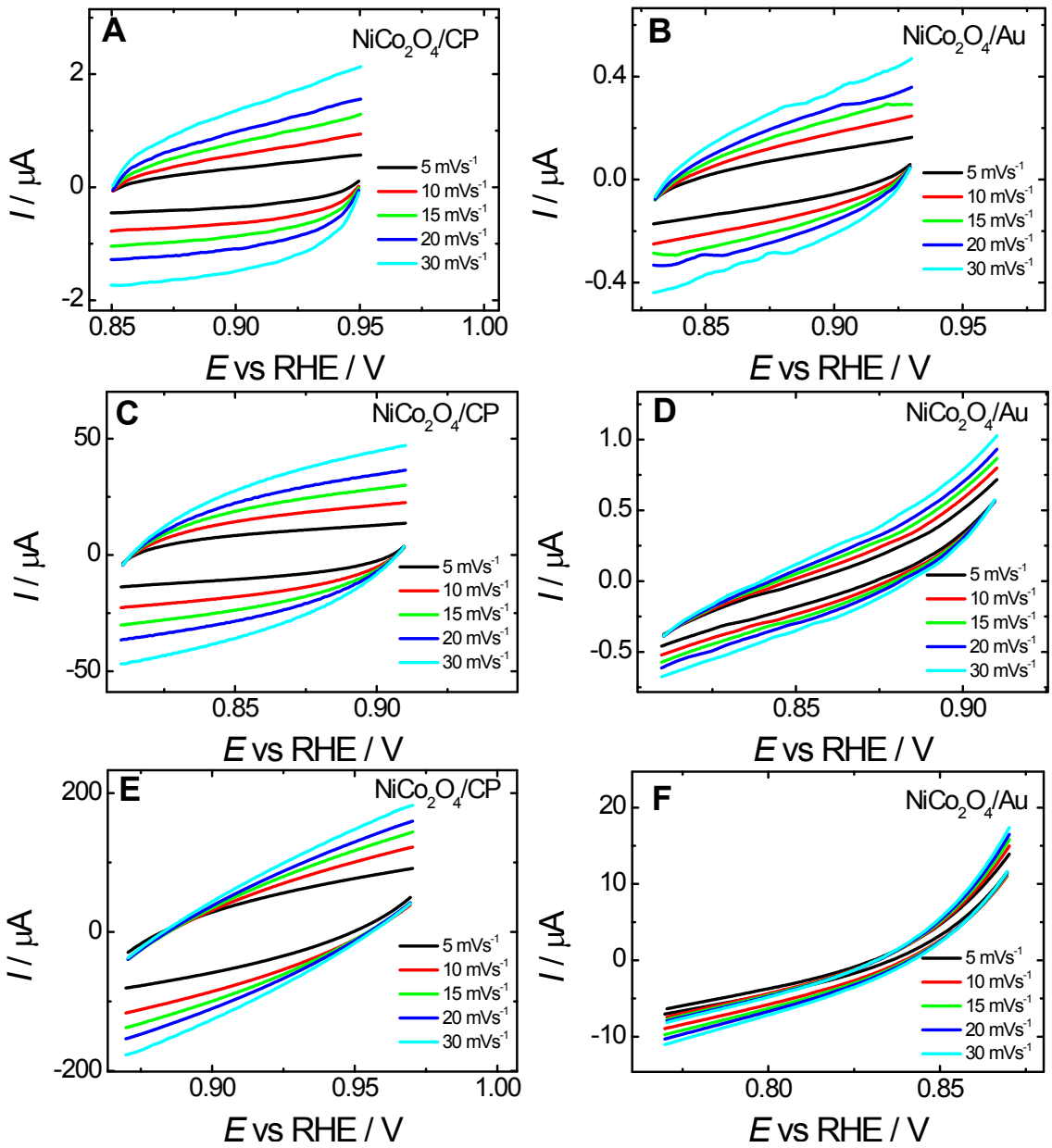

Figure S12. Cyclic voltammograms measured in a non-Faradaic potential region—also comprising the open circuit potential (OCP)—for different modified electrodes in N_2-saturated 1 M KOH before OER (A and B), after OER (C and D), and after OER stability test (E and F). The modified electrodes were kept in each vertex potential for 10 sec before starting the next potential sweep. Scans started at higher potentials.

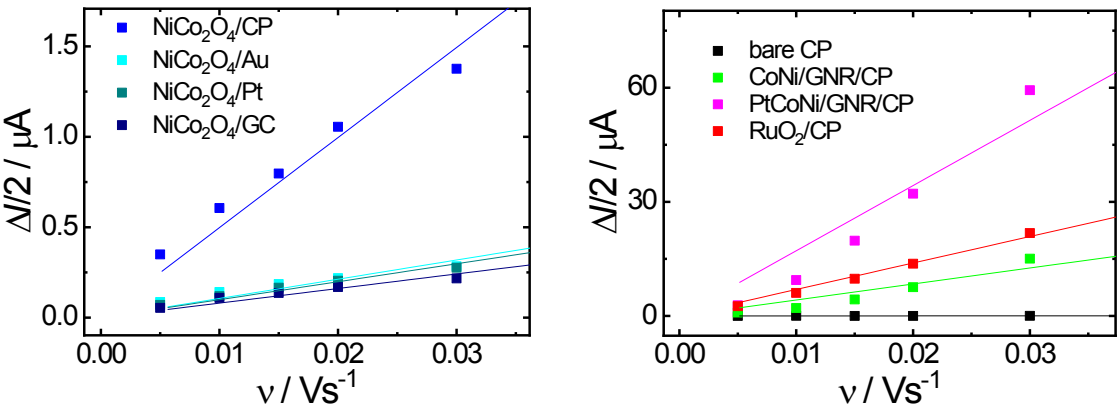

Figure S13. Plots related to the differences between anodic and cathodic double layer charging currents (Figure S12A-B, before OER) divided by 2 (($\Delta I = I_a – I_c$)/2), measured in the OCP, which is also in a non–Faradaic potential region, relative to the potential scan rates. The slopes of these plots result in a double–layer capacitance ($C_{dl} = \frac{\frac{\Delta I}{2}}{\nu}$) values (see Table S6) used for determining electrochemically active surface areas ($ECSA = \frac{C_{dl}}{C_s}; C_s = 0.040\ mF\ cm^{-2}\ in\ 1\ M\ KOH$ [19]) for different modified electrodes in N_2-saturated 1 M KOH.

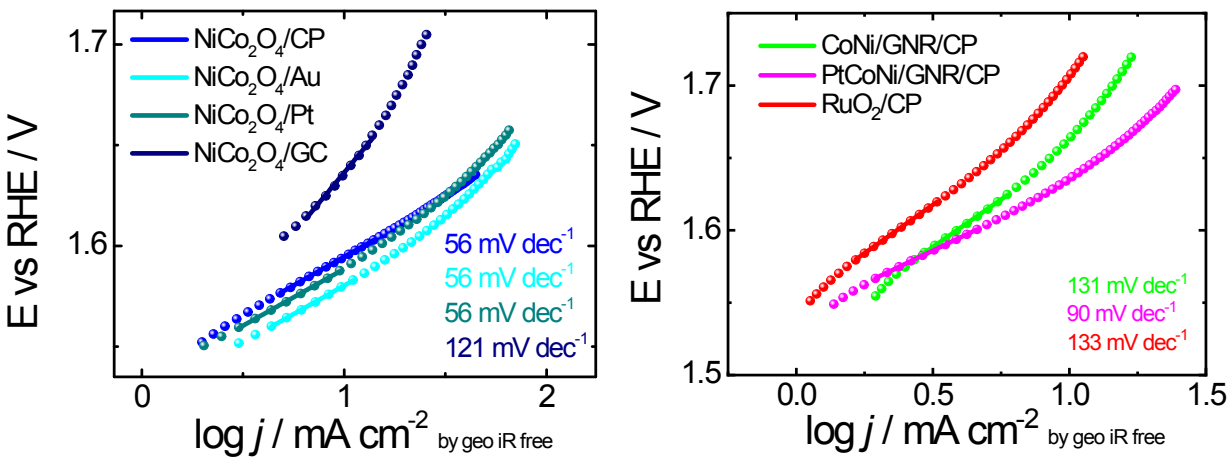

Figure S14. Tafel plots based on the data (during OER) from Figures 3B, S7B, and S7D for bare and different modified electrodes in O_2-saturated 1.0 M KOH.

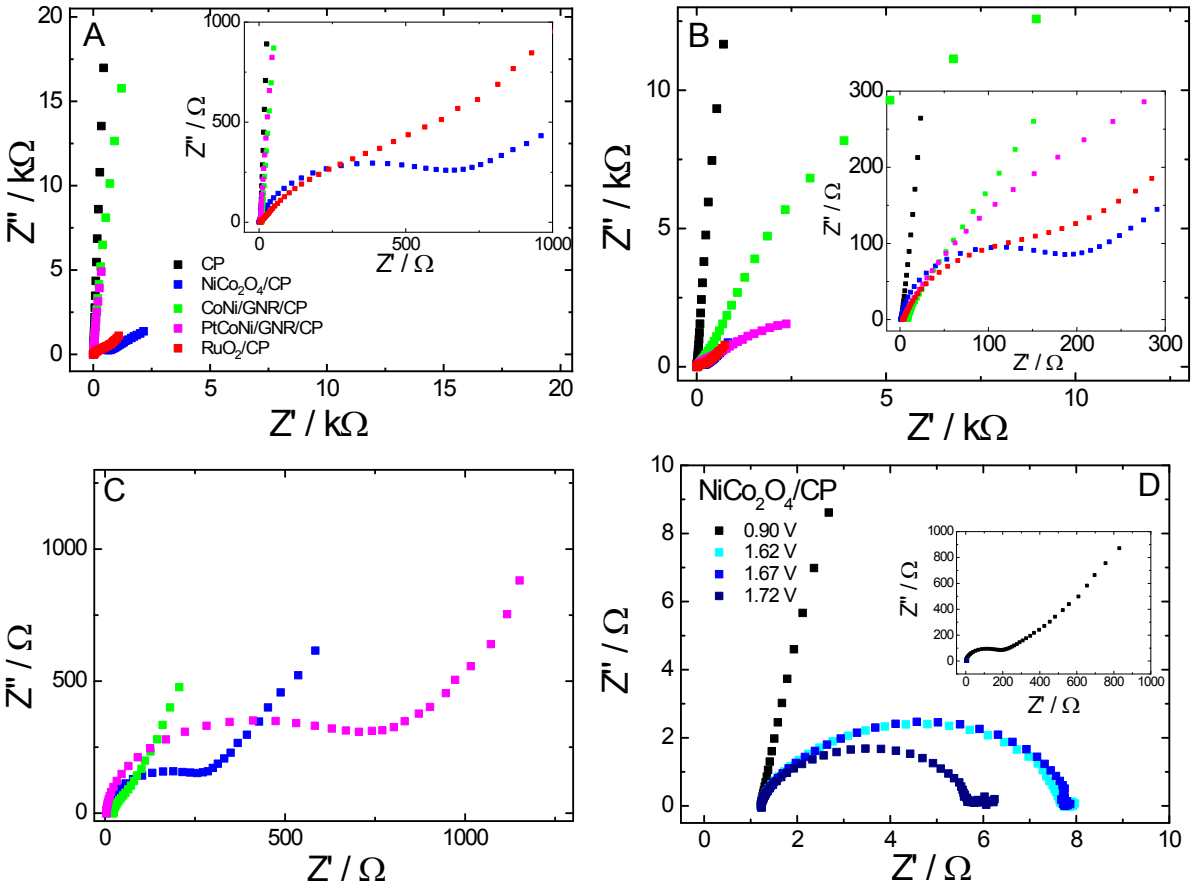

Figure S15. EIS results related to (A) initial electrochemical measurements, (B) after OER measurements, and (C) after OER long-term stability test, for bare and different modified CP electrodes, and (D) for $NiCo_2O_4$/CP electrode at different potentials without iR compensation (0.90 V = OCP, and 1.62, 1.67, and 1.72 V = potential, where the densities: 5, 10, and 20 mA $cm^{-2}_{by\ geo}$, respectively) are obtained in N_2-saturated 1.0 M KOH solution. Potential perturbation: 10 mV (rms). Frequency range: 100 kHz–10 mHz. Constant potential for EIS acquisition: OCP ((A) 0.96, (B) 0.86, and (C) 0.85 V *vs.* RHE on average). Inset: Impedance plane plots restricted to (A) 1000, (B) 300, and (D) 1000 Ω. The R_u value used for iR compensation in Figures 3B and S7D was 3.7 Ω on average.

Table S8 – Values related to content, C_{dl} – obtained from CV responses (Figure S16), ECSA – obtained from (Figure S17), $E_{1/2}$ = potential at half limiting current density values (Figures 3D and S7F), n_{K-L} = number of electrons obtained from Kouteck-Levich plot (Figure S18), % HO_2^- = peroxide percentage (Figure S19), and Tafel slope for modified electrodes (Figure S20).

Electrode	Content ($\mu g\ cm^{-2}$)	C_{dl} (μF)			ECSA (cm^2)			$E_{1/2}$ (V)	n_{K-L}	% HO_2^-	Tafel slope ($mV\ dec^{-1}$)	
		Initial	After RRO	After RRO stability	Initial	After RRO	After RRO stability					
Pt(20%)C/GC	150	450	511	–	11.3	12.8	–	0.87	3.9	17	–64	–144
PtCoNi/GNR/GC	150	636	625	378	15.9	15.6	9.4	0.80	3.6	34	–60	–253
PtCoNi/GNR'/GC	250	1,110	1,190	1,790	27.8	29.8	44.6	0.82	3.6	20	–60	–253
CoNi/GNR/GC	150	168	209	–	4.2	5.2	–	0.81	2.8	34	–41	–332
CoNi/GNR'/GC	250	396	446	–	9.9	11.2	–	0.79	2.8	34	–39	–255
$NiCo_2O_4$/GC	150	5.8	5.7	–	0.14	0.14	–	0.65	2.2	78	–67	–
GNR/GC	150	940	852	–	23.5	21.3	–	0.74	2.3	59	–64	–289

Table S9. Summary for PtCoNi/GNR ORR activity reported in the present work and earlier literature for other catalysts.

Catalyst	$E_{1/2}$ (V)	Loading (μg cm^{-2})	Mass activity at 0.85 V (mA μg^{-1})	Specific activity at 0.85 V (mA cm^{-2}	Solution	n	Tafel slope (mV dec^{-1})	Ref.
PtCoNi/GNR'	0.82	250	0.19	0.01	0.1 M KOH	3.9	–64 –144	**Present study**
Hierarchical $NiCo_2O_4$ hollow nanospheres	Not reported	400	Not reported	Not reported	0.1 M KOH	3.0-4.0	–67 –102	[16]
CoNi@N−C	0.82	250	Not reported	Not reported	0.1 M KOH	3.8	–56.9 to –69.1	[20]
N-doped carbon stabilized Co−Pt bimetallic nanoalloys	0.87	125	35.3 (0.8 V)	4.5 mA cm^{-2} (0.8 V)	0.1 M KOH	4.0	–66	[21]
NiCo@GC	0.81	500	Not reported	Not reported	0.1 M KOH	3.9	–52.1	[22]
A-CoPt-NC	0.96	318	45.47 (0.9 V)	1.41 (0.9 V)	0.1 M KOH	3.7	Not reported	[23]
Co/N-PCNF	0.87	250	Not reported	Not reported	0.1 M KOH	3.9	–99.3	[24]
$NiCo_2O_4$-rGO hybrid nanosheets	Not reported	400	Not reported	Not reported	0.1 M KOH	3.8	Not reported	[25]
Mesoporous $NiCo_2O_4$ nanoplate	~0.86	400	0.075	Not reported	0.1 M KOH	4.0	–51	[26]
Three-dimensional (3D) macroporous $NiCo_2O_4$ sheets	Not reported	804	0.001 (–0.1 V vs. Ag/AgCl)	Not reported	0.1 M KOH	3.8	Not reported	[27]
C/$NiCo_2O_4$	0.59 V vs. Ag/AgCl	113.2	Not reported	Not reported	0.1 M KOH	3.9	Not reported	[28]
Spinel $NiCo_2O_4$	0.82	Not reported	Not reported	Not reported	1 M NaOH	4.0	–52 –179	[29]

CoNi@N−C = porous N-doped carbon-encapsulated CoNi alloy nanoparticle composite; NiCo@GC = graphitic carbon-supported NiCo alloys; A-CoPt-NC = atomic Pt–Co nitrogen-carbon-based catalyst; Co/N-PCNF = cobalt, nitrogen dual-doped porous carbon nanosheet-assembled flowers; C/$NiCo_2O_4$ = carbon supported nickel cobaltite nanofibers.

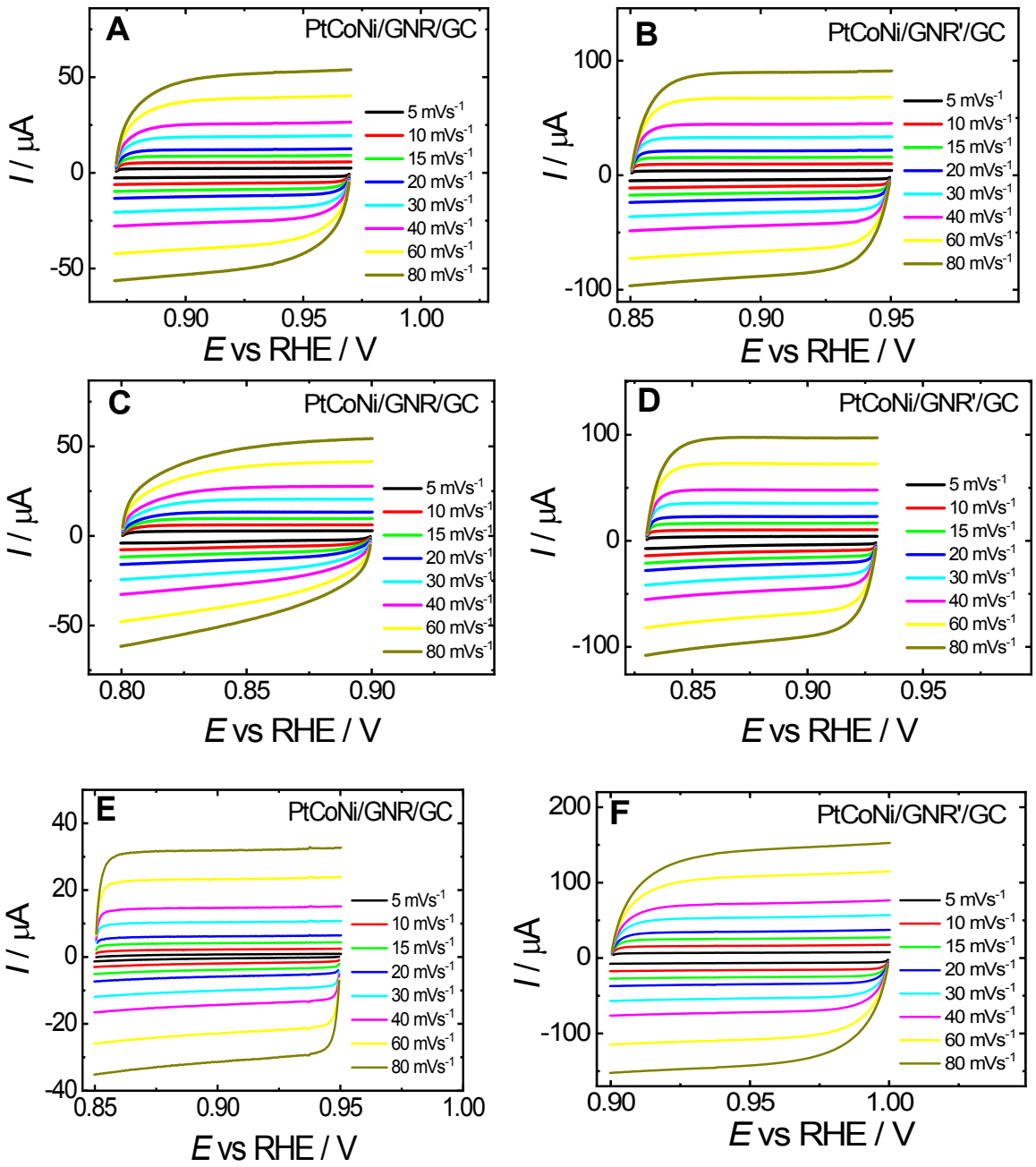

Figure S16. Cyclic voltammograms measured in a non-Faradaic potential region—also involving the OCP—under different contents (see Table S8) for modified electrodes in N_2-saturated 0.1 M KOH before ORR (A and B), after ORR (C and D), and after stability test for ORR (E and F). The modified electrodes were kept in each vertex potential for 10 sec before starting the next potential sweep. Scans started at higher potentials.

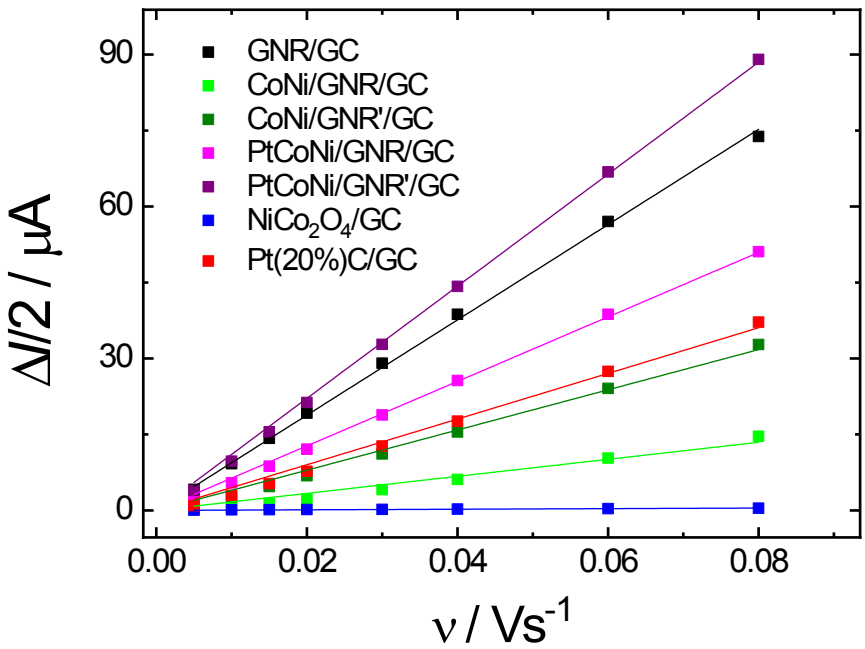

Figure S17. Plots related to the differences between anodic and cathodic double layer charging currents (Figure S16A-B, before ORR) divided by 2 ((ΔI = I_a–I_c)/2), measured in the OCP, which is also in a non–Faradaic potential region, as a function of potential scan rates. The slopes of these plots result in C_{dl} values (see Table S8) used for determining $ECSA$ ($C_s = 0.040\ mF\ cm^{-2}$ [19] $also\ considered\ for\ 0.1\ M\ KOH$) for different modified electrodes in N_2-saturated 0.1 M KOH.

Specific activity (SA) = (((I × I_d)/(I_d – I))= I_k/ECSA [30] (S1)

where I is the measured current at 0.8 or 0.85 V and I_d and I_k are the diffusion–limited and kinetic currents, respectively.

Mass activity (MA) = I_k/(L_{PGM} × A_{geo}) [30] (S2)

where A_{geo} is the geometric GC surface area (cm^2) and L_{PGM} is the Pt–group metal content of the working electrode (mg cm^{-2}).

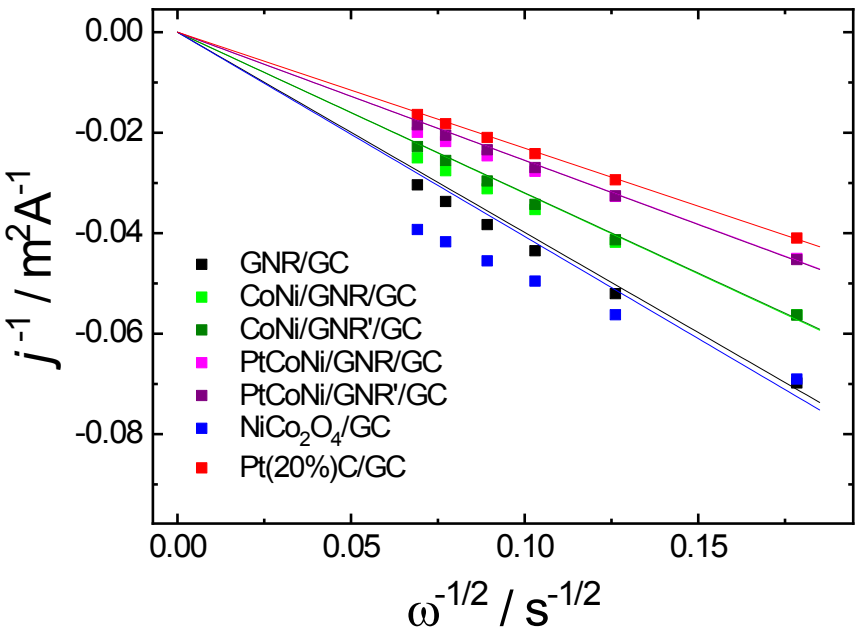

Figure S18. Koutecký – Levich curves ($1/(j_{lim} = I_{lim}$ disc/geometric area of the disk)) vs. $\omega^{-1/2}$) obtained from the curves as shown in Figures 3D and S7F (obtained in different rotation rates) at 0.3 V, and specifically at 0.4 V for the Pt/C/GC electrode.

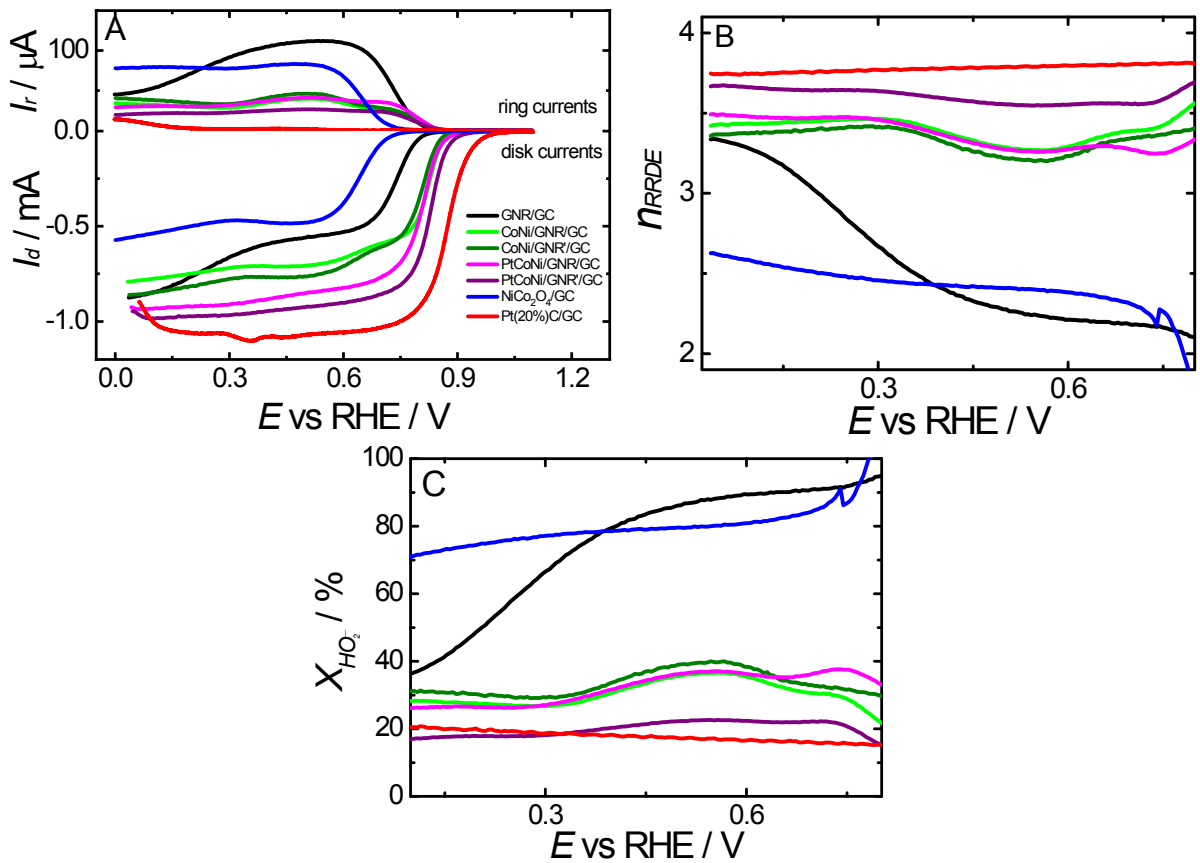

Figure S19. (A) Hydrodynamic linear scan (HLS) curves for different modified electrodes obtained in O_2-satured 0.1 M KOH. Scan rate: 5 mV s^{-1} and ω=1600 rpm. Scans started at 0.00 V. The ring current responses for the bare Pt ring were obtained by maintaining this electrode at 1.1 V in O_2 saturated 0.1 M KOH, while the potentials on the modified GC disk electrodes were scanned in the same solution at different ω values and 5 mV s^{-1}. (B) Numbers of transferred electrons obtained using rotating ring-disk electrodes (RRDE) responses (A) (n_{RRDE}) for different modified disk electrodes during ORR at different potentials and (C) percentages of hydrogen peroxide production (% HO_2^-). Values of n_{RRDE} and % HO_2^- were obtained from the corresponding HLS data at 1600 rpm based on (A) and obtained by equations S3−S6.

The HO_2^- production ($X_{HO_2^-}$ in terms of percentage) was calculated using molar flow rates of O_2 ($\dot{n}_{O_{2(4e^-)}}$) and HO_2^- ($\dot{n}_{O_{2(2e^-)}}$), using Equations S3 and S4 [31-33].

$$\dot{n}_{O_{2(4e^-)}} = \frac{I_{H_2O}}{4F} \text{ e } \dot{n}_{O_{2(2e^-)}} = \frac{I_{HO_2^-}}{2F} \qquad \text{Equation S3}$$

$$\% HO_2^- = X_{HO_2^-} = \frac{\dot{n}_{O_{2(2e^-)}}}{\dot{n}_{O_{2(2e^-)}} + \dot{n}_{O_{2(4e^-)}}} = \frac{\frac{2I_r}{N}}{I_d + \frac{I_r}{N}}$$

Equation S4

where $I_{H_2O} = I_d - I_{HO_2^-}$, $I_{HO_2^-} = I_r N^{-1}$, $N = -\frac{I_r}{I_d}$, and $\frac{I_d}{n_{e^-}} = \frac{I_{H_2O}}{4} + \frac{I_{HO_2^-}}{2}$, I_{H_2O} and $I_{HO_2^-}$ are the O_2 reduction currents for water and HO_2^-, respectively, F is the Faraday constant (96 485 C mol^{-1}); I_r e I_d are the Pt ring and modified GC disk currents, respectively, and N is the collection efficiency value obtained experimentally.

The number of electrons (n_{RRDE}) involved in the ORR was obtained using the following equation [31-33]:

$$n_{RRDE} = \frac{4I_d}{I_d + I_r/N}$$

Equation S5

The collection efficiency (N) needs to be calibrated for each experiment, considering the great influence of content and roughness of the catalyst, as well as the rotating rate of the electrode. The currents of the Pt ring electrode kept at 1.6 V were measured during the hydrodynamic voltammetry at various ω for modified electrodes, in 0.1 M KOH N_2-saturated, containing 1 mM of $K_3[Fe(CN)_6]$. The N value was calculated using Equation S6 [31-33].

$$N = \frac{I_r}{I_d}$$

Equation S6

where I_r and I_d are the Pt ring and modified GC disk currents, respectively.

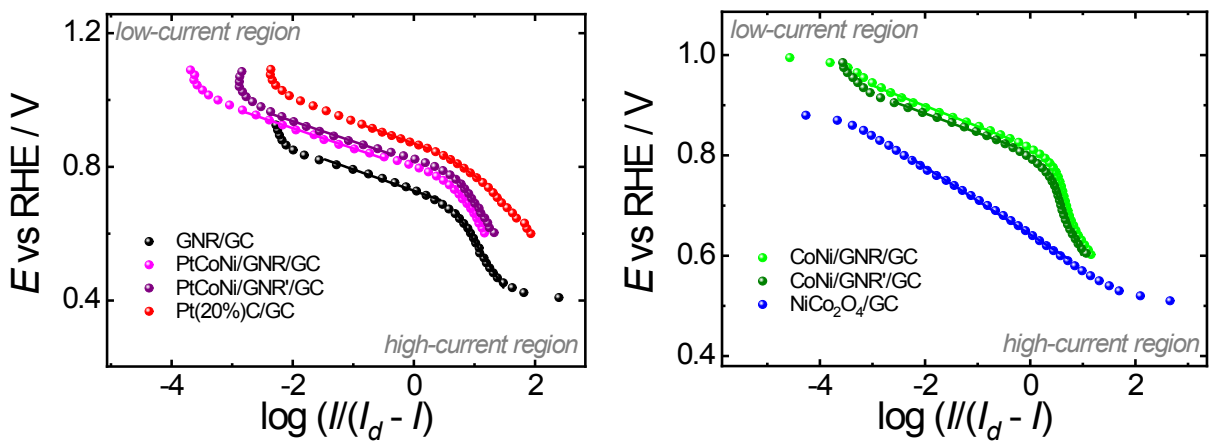

Figure S20. Tafel plots based on the data (during ORR) from Figures 3D, S7F, and S19A for different modified electrodes in O_2-saturated 0.1 M KOH.

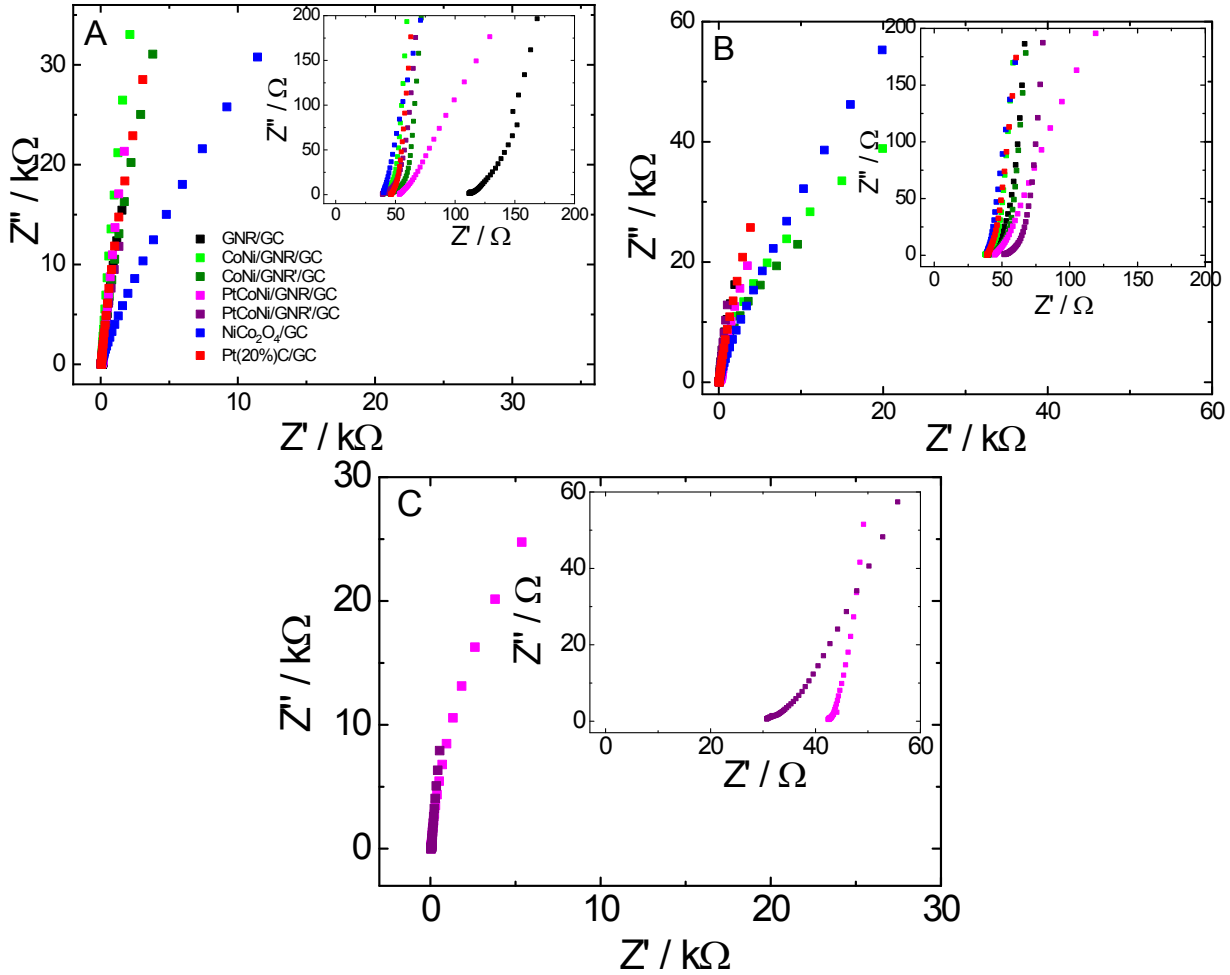

Figure S21. EIS results related to (A) initial electrochemical measurements, (B) after ORR, and (C) after ORR long-term stability test for different modified GC electrodes obtained in N_2-saturated 0.1 M KOH solution. Potential perturbation: 10 mV (rms). Frequency range: 100 kHz–10 mHz. Constant potential for EIS acquisition: OCP ((A) 0.92; (B) 0.88 V and (C) 0.92 V *vs.* RHE on average). Inset: Impedance plane plots restricted to (A) 200, (B) 200 Ω and (C) 60 Ω. The R_u value used for iR compensation in Figures 3D and S6F was 56.1 Ω on average.

References

[1]. L. Yang, B. Zhang, B. Fang, L. Feng, *Chemical Communications,* 2018, **54**, 13151–13154.
[2] B. Cui, H. Lin, J.-B. Li, X. Li, J. Yang, J. Tao, *Advanced Functional Materials,* 2008, **18**, 1440–1447.
[3] R. Chen, H.-Y. Wang, J. Miao, H. Yang, B. Liun, *Nano Energy*, 2015, **11**, 333–340.
[4] J. Wang, T. Qiu, X. Chen, Y. Lu, W. Yang, *Journal of Power Sources,* 2014, **268**, 341–348.
[5] Y.-Z. Su, Q.-Z. Xu, G.-F. Chen, H. Cheng, N. Li, Z.-Q. Liu, *Electrochimica Acta* **2015**, *174*, 1216–1224.
[6] C. Chang, L. Zhanga, C.-W. Hsu, X.-F. Chuah, S.-Y. Lu, , *ACS Applied Materials & Interfaces*, 2018, **10**, 417–426.
[7] C. Zhu, S. Fu, D. Du, Y. Lin, *Chemistry —A European Journal*, 2016, **22**, 4000–4007.
[8] Z. Li, B. Li, J. Chen, Q. Pang, P. Shen, *International Journal of Hydrogen Energy*, 2019, **44**, 16120–16131.
[9] C. Luan, G. Liu, Y. Liu, L. Yu, Y. Wang, Y. Xiao, H. Qiao, X. Dai, X. Zhang, *ACS Nano,* 2018, **12**, 3875−3885.
[10] Y. Gong, Z. Yang, Y. Lin, J. L. Wang, H. Pana, Z. Xu, *Journal of Materials Chemistry A* 2018, **6**, 16950–16958.
[11] M. Yang, W. Lu, R. Jin, X.-C. Liu, S. Song, Y. Xing, *ACS Sustainable Chemistry & Engineering*, 2019, **7**, 12214−12221.
[12] Y. Wang, Z. Zhang, X. Liu, F. Ding, P. Zou, X. Wang, Q. Zhao, H. Rao, *ACS Sustainable Chemistry & Engineering,* 2018, **6**, 12511−12521.
[13] H. Fu, Y. Liu, L. Chen, Y. Shi, W. Kong, J. Hou, F. Yu, T. Wei, H. Wang, X. Guo, *Electrochimica Acta,* 2019, **296**, 719−729.
[14] Y. Liu, P. Liu, W. Qin, X. Wu, G. Yang, *Electrochimica Acta,* 2019, **297**, 623–632.
[15] S. Sun, X. Jin, B. Cong, X. Zhou, W. Hong, G. Chen, *Journal of Catalysis,* 2019, **379**, 1–9.
[16] J. Wang, Y. Fu, Y. Xu, J. Wu, J.-H. Tian, R. Yang, *Internation Journal of Hydrogen Energy*, 2016, **41**, 8847-8854.
[17] C. Broicher, F. Zeng, J. Artz, H. Hartmann, A. Besmehn, S. Palkovits, R. Palkovits, *ChemCatChem,* 2019, **11**, 412–416.
[18] 3. Z. Chen, B. Zhao, Y.-C. He, H.-R. Wen, X.-Z. Fu, R. Sun, C.-P. Wong, *Materials Chemistry Frontiers,* 2018, **2**, 1155–1164.
[19] C. C. L. McCrory, S. Jung, J. C. Peters, T. F. Jaramillo, *Journal of the American Chemical Society,* 2013, **135**, 16977−16987.
[20] H. Ning, G. Li, Y. Chen, K. Zhang, Z. Gong, R. Nie, W. Hu, Q. Xia, *ACS Applied Materials & Interfaces,* 2019, **11**, 1957-1968.
[21] L.-L. Ling, W.-J. Liu, S.-Q. Chen, X. Hu, H. Jiang, *ACS Applied Nano Materils,* 2018, **1**, 3331−3338.
[22] A. Sivanantham, S. Shanmugam, *ChemElectroChem*, 2018, **5**, 1937–1943.
[23] L. Zhang, J. M. T. A. Fischer, Y. Jia, X. Yan, W. Xu, X. Wang, J. Chen, D. Yang, H. Liu, L. Zhuang, M. Hankel, D. J. Searles, K. Huang, S. Feng, C. L. Brown, X. Yao, *Journal of the American Chemical Society,* 2018, **140**, 10757−10763.
[24] S. Chen, Y. Zheng, B. Zhang, Y. Feng, J. Zhu, J. Xu, C. Zhang, W. Feng, T. Liu, *ACS Applied Materials & Interfaces*, 2019, **11**, 1384−1393.
[25] G. Zhang, B. Y. Xia, X. Wang, X. W. (D.) Lo, *Advanced Materials,* 2014, **26**, 2408–2412.
[26] X. Tong, S. Chen, C. Guo, X. Xia, X.-Y. Guo, *ACS Applied Materials & Interfaces,* 2016, **8**, 28274–28282.
[27] Y. Xiao, C. Hu, L. Qu, C. Hu, M. Cao, *Chemistry—A European Journal,* 2013, **19**, 14271–14278.

[28] D. Hassan, S. El-safty, K. A. Khalil, M. Dewidar, G. A. El-magd, *Materials,* 2016, **9**, 759 (1–15).
[29] S. V. Devaguptapu, S. Hwang, S. Karakalos, S. Zhao, S. Gupta, D. Su, H. Xu, G. Wu, *ACS Applied Materials & Interfaces,* 2017, **9**, 44567–44578.
[30] C. V. Boone, G. Maia, *Electrochimica Acta,* 2017, **247**, 19–29.
[31] E. S. F. Cardoso, G. V. Fortunato, G. Maia, *ChemElectroChem,* 2018, **5**, 1691–1701.
[32] E. S. F. Cardoso, G. V. Fortunato, G. Maia, *The Journal of Physical Chemistry C,* 2019, **123**, 16308–16316.
[33] E. S. F. Cardoso, G. V. Fortunato, I. Palm, E. Kibena-Põldsepp, A. S. Greco, J. L. R. Júnior, A. Kikas, M. Merisalu, V. Kisand,V. Sammelselg, K. Tammeveski, G. Maia, *Electrochimica Acta,* 2020, **344**, 136052.